Mechanical Design of a Cubesat Aeroshell for an Earth Demonstration of Single-Stage Drag Modulated Aerocapture

AE 8900 MS Special Problems Report
Space Systems Design Laboratory (SSDL)
Guggenheim School of Aerospace Engineering
Georgia Institute of Technology
Atlanta, GA

Author:
Bryce A. Woollard

Advisor:
Dr. Robert D. Braun

August 5, 2016

Mechanical Design of a Cubesat Aeroshell for an Earth Demonstration of Single-Stage Drag Modulated Aerocapture

Bryce A. Woollard[1] and Robert D. Braun[2]
Georgia Institute of Technology, Atlanta, GA 30332

The following article documents the conceptual study of a smallsat entry vehicle to be implemented for demonstration of single-stage drag modulated aerocapture at Earth. The specific nature of the contents below focuses on the mechanical design and analysis of the aeroshell and drag device, as well as the mechanisms by which all parts are to be manufactured, assembled and actuated in order to perform the intended orbital maneuver. The results of this study show that accomplishing aerocapture with a cubesat entry vehicle appears to be feasible with a 2U payload and would require approximately 20 kg and 0.1 m^3 of secondary payload mass and volume, respectively. First order stagnation point thermal protection sizing suggests that 4.2 cm of PICA would be required globally around the vehicle, although potential exists to optimize this value relative to geometric location. Static stability analysis indicates that the designed vehicle is nose-forward stable for a majority of the atmospheric interface with outstanding questions pertaining to atmospheric egress. Manufacturing costs for a full scale aeroshell would be approximately $15,000 and require roughly 2 months of lead time, dependent on presently available machine shop capabilities.

Nomenclature

β = ballistic coefficient

m = mass

C_DA = drag area

β_1 = pre-jettison ballistic coefficient

β_2 = post-jettison ballistic coefficient

[1] Graduate Research Assistant, Daniel Guggenheim School of Aerospace Engineering
[2] Professor, Daniel Guggenheim School of Aerospace Engineering, AIAA Fellow

r = foreshell radius

R = drag skirt radius

r_n = foreshell nose radius

r_s = foreshell shoulder radius

ψ = backshell taper angle

L_1 = foreshell axial length

L_2 = backshell axial length

θ = foreshell conical half angle

t = thickness

$\hat{x}$ = static margin

C_p = pressure coefficient

P_∞ = freestream static pressure

q_∞ = freestream dynamic pressure

P = local static pressure

$\dot{q}$ = local heat flux

$\dot{q}_{stag}$ = stagnation point heat flux

K = Sutton Graves constant

ρ_∞ = freestream density

V_∞ = freestream velocity

X = longitudinal backshell distance from foreshell interface

h = foreshell outer diameter to backshell outer diameter radial step distance

C_{m_α} = pitching moment stability derivative

I. Introduction

In the field of planetary exploration, orbital transfer maneuvers exist in order to alter a spacecraft's trajectory either when navigating deep space or when approaching a target. In most cases, these maneuvers rely upon one or many propulsive exercises to alter the vehicle's attitude or velocity such that the gravitational forces exerted by the target body can either detour or capture the spacecraft, dependent upon the mission at hand. While retropropulsive maneuvers are reliable and almost explicitly used to accomplish this task, an alternative approach to this challenge exists; missions that lie under this category are called *aeroassist missions*. Aeroassist missions aim to minimize unnecessary launched mass and volume of a spacecraft by relying upon the target body's atmosphere to create lift and drag forces which alter the spacecraft's trajectory profile rather than solely relying upon propulsion. While the necessary drag surfaces to accomplish an aeroassist type mission have their own set of stringent design requirements, they have a much greater mass savings potential due to the presently available material selections and lightweight nature of the system relative to the equivalent propulsion system required to obtain an appropriate ΔV. Aeroassist missions can be more clearly defined based on the specifics of the maneuver; one such maneuver that falls under the broader spectrum of aeroassist type missions is called *aerocapture*. In short, the purpose of aerocapture is to transfer from a hyperbolic trajectory to an elliptic trajectory of a target body by means of a single pass through the atmosphere followed by two small ΔV maneuvers at apoapsis and periapsis. This task is accomplished by directly entering the target body's atmosphere and utilizing atmospheric lift and drag to dissipate kinetic energy and decrease the vehicle's relative velocity until escape velocity is obtained; at this point, the vehicle then exits the atmosphere and continues along a transfer orbit until apoapsis, at which time a single ΔV raise maneuver is employed to make sure that the spacecraft doesn't pass through the atmosphere at periapsis. Once the spacecraft reaches periapsis, a second small ΔV maneuver is employed to set into the target orbit; Figure 1 displays the sequence of events which occur during a typical aerocapture mission.

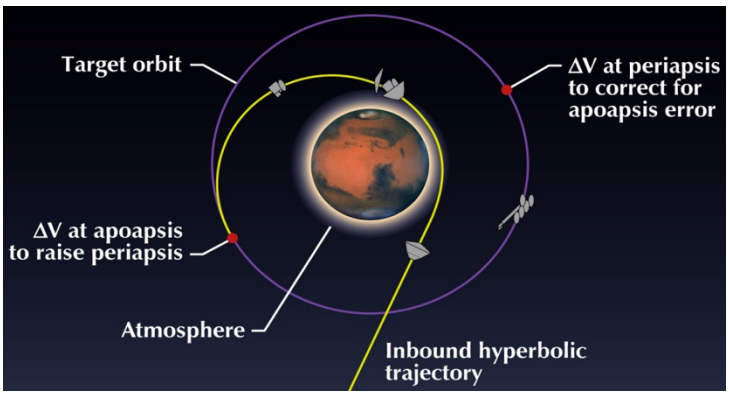

Figure 1. Aerocapture Mission Sequence.

While the concept of aerocapture has been studied in great depth since the 1950's, to this point in time it has yet to be demonstrated for a planetary entry. Some claim that the Apollo CM flew a trajectory which included aspects of aerobraking (repeated passes through the atmosphere to dissipate energy); however, no missions to date have employed aerocapture as the primary orbit transfer maneuver during the transition from a hyperbolic to an elliptic orbit. Past proposals have been submitted which attempted to include an aerocapture demonstrator as either the primary mission or as a secondary payload to a larger mission; however, the amount of risk and cost associated with including additional mission requirements and launched mass led to these proposals being cut from flight plans.

In general, the ability to utilize aerocapture as the primary orbital transfer maneuver provides a very advantageous opportunity for planetary exploration. For relatively near Earth missions, the amount of fuel and structure mass required for a retropropulsive system can instead be utilized for payload. Additionally, the capability to package a deployable system with a modular drag area and actuate either exo-atmospherically or during atmospheric entry eases constrains imposed from launch vehicle fairing diameters and increases landing maneuverability and landing accuracy. These opportunities fall directly in line with the many near future challenges that exist for the human exploration of Mars. For missions which intend to explore planets further away from Earth in the Solar System (Uranus, Neptune, Pluto) where very high Earth exit velocities are required, aerocapture not only becomes a mass savings opportunity but instead becomes a mission enabler for orbiters at these locations due to the limitations which exist for retropropulsive systems.

It is clear to see the potential benefits of employing an aerocapture system for planetary orbit entry. Due to the previous difficulties of including secondary payload aerocapture hardware, a concept has been conceived which proposes for aerocapture to be demonstrated on Earth with a very cheap, simple, and straight-forward entry vehicle.

II. Approaches to Aerocapture Execution

As explained in the introduction, aerocapture poses a wide variety of opportunities for planetary exploration; there are however many ways to go about accomplishing aerocapture during flight. While the work performed by Dr. Zachary Putnam in [1] and [2] details the theory behind various approaches to accomplishing aerocapture, two fundamental architectures exist which pose their own benefits and shortcomings. It is important to first define the ballistic coefficient (β), presented in Equation 1. Fundamentally, it can be described as the ratio of inertial to aerodynamic drag forces acting on an entry vehicle.

$$\beta = \frac{m}{C_D A} \tag{1}$$

This term appears numerous times throughout the governing equations of motion for a 3 DOF entry vehicle, and is a primary contributor to the spacecraft's trajectory. The first architecture relies upon a modular system with which the magnitude of the vehicle's lift or bank angle is altered by means of either a CG offset or geometric alteration. While this poses benefits in the realm of landing accuracy, heat rate/heat load minimization, and trajectory optimization, it requires a much more complex and costly system. The focus of the following document will be primarily on a secondary architecture where a non-lifting (ballistic) trajectory is utilized and all terms in the governing equations of motion related to lift disappear. Eliminating these terms leaves the aforementioned ballistic coefficient as one of the last remaining alterable parameters with which to perturb the spacecraft's trajectory. Aeroassist missions which alter the drag area and ballistic coefficient of the entry vehicle are called *drag modulated aerocapture missions*. This alteration of the drag area and ballistic coefficient can be performed either as a function of time or at a discrete point in the trajectory. The aim of this study was to examine the feasibility of performing a discrete event drag modulated aerocapture at Earth using a very simple system aboard a secondary payload 2U (10 cm x 10 cm x 20 cm) cubesat. The modulation in drag was to be accomplished by means of jettisoning a rigid drag skirt, consequently changing the vehicle's ballistic coefficient during atmospheric interface. Following atmospheric egress, the two ΔV maneuvers would then be performed to place the cubesat into the desired parking orbit, where on-board IMU data could then be transmitted to a host vehicle. Figure 2 below displays the mission aspects included in a single-stage drag modulated aerocapture sequence.

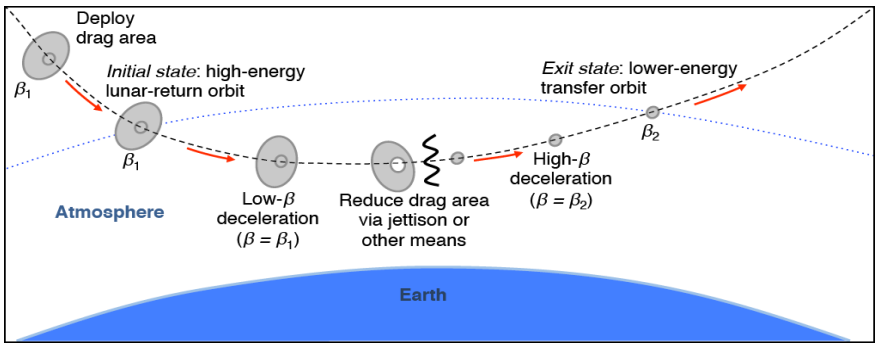

Figure 2. Single-Stage Drag Modulated Aerocapture Mission Sequence.

III. Aeroshell Design Requirements

The first step in any successful design process is to clearly define and understand the requirements of the mission at hand. As a primary subassembly to an entry vehicle, the aeroshell has many critical design parameters that must be accounted for in order to provide mission success. The harsh environments associated with exo-atmospheric exposure and hypersonic atmospheric entry expose the vehicle to both very low and very high temperatures, as well as vibrations and unsteady structural loads. While the severity of these loads is much greater for a complete entry mission, they do still exist for aeroassist missions and directly impact how the aeroshell design is conducted. In addition to the environmental factors, launch vehicle rideshare mass and volume constraints drive the aeroshell design and set parametric limits on geometric and material selections. The most influential limit driving this particular aeroshell design was that of the launch vehicle and the restrictions set on rideshare volume (1 m x 0.5 m x 0.4 m); these dimensions drove the limits for the drag skirt outer radius, as well as the longitudinal chord of the vehicle. Additionally, the goal ballistic coefficient ratio for the pre and post-jettison configurations dictated the geometric aeroshell dimensions, as discussed in the following section.

IV. Aeroshell Geometry Selection

In conjunction with the previously defined mission requirements, conceptual design of the aeroshell began with the selection of a forebody shape. The initial trade study considered 45°, 60° and 70° sphere cone half angles; due to its forgiving characteristics concerning heating, drag and stability [3], the 60° blunted cone was selected. It had been employed for a wide variety of missions and tests, many of which were for small probe missions either at Earth

(Genesis, Stardust) or beyond (Beagle 2, Huygens) and plentiful historical data on supersonic and hypersonic testing of 60° blunted cones was available, as referenced throughout this document. Knowing that the ballistic coefficient ratio $\left(\frac{\beta_2}{\beta_1}\right)$ between the pre and post-jettison configurations was desired to be somewhere between 5 and 10, and that the launch vehicle rideshare constraints restricted the maximum dimensions of the aeroshell to be (1 m x 0.5 m x 0.4 m), the outer radius of the rigid drag skirt (R) was selected to be 25 cm while the inner foreshell radius (r) was selected to be 10 cm, yielding a goal ballistic coefficient ratio of $\frac{\beta_2}{\beta_1} \approx \mathbf{5.6}$. In addition to the conical half angle, nose radius and shoulder radius values were selected to be $\mathbf{r_n} = \frac{9}{16}\mathbf{r}$ and $\mathbf{r_s} = \frac{1}{10}\mathbf{r_n}$, respectively, taken from heritage values (Genesis, Stardust) and expert recommendations.

The backshell underwent multiple iterations due to stability concerns (Section V); however, the most recent iteration was designed to accommodate a 2U rectangular prism payload oriented along the longitudinal axis. The backshell tapers from its interface with the foreshell to its aft surface by an angle of ψ = 5.3° and measures 21 cm from the foreshell interface to its aft plane. The conical taper was included to mitigate static stability concerns, drive the CG forward and reduce backshell drag to a near optimal value [4]. Further explanation of the entire aeroshell and drag skirt design is provided in the following sections.

V. CAD Design

Prior to beginning the CAD design process, it was designated a primary goal to maintain simplicity of the aeroshell design such that extraneous metal work was not required and that all parts could be manufactured for a low cost, quickly and easily. This notion was derived directly from the higher level goal of preserving mission minimalism by use of a cubesat entry vehicle and being able to demonstrate aerocapture with a very straightforward set of on-board instrumentation and payload features.

Following up on the foreshell, backshell and drag skirt geometry justifications explained in the previous section, the foreshell was designed as a 3 mm (~0.125”) thick 6061 aluminum sphere cone with four orthogonally spaced mating bosses for the foreshell / backshell joint. Sufficient volume was left in the interior base of the nose such that ballast could be added to drive the CG further forward and alleviate potential stability challenges. Four aft-driven counterbored fastener holes for M3 / 6 mm socket cap screws were included such that the screw cap heads could live entirely below the outer mold line of the aeroshell and thermal protection system (TPS) material could be used as a

filler immediately prior to deployment. Due to the fact that shear loading between the two aeroshell components was presumably small, and that each boss included a 1 mm male / female notch to carry shear load and ease assembly challenges, the M3 fasteners were selected primarily due to the fact that M3 fasteners were also the fastener of choice for the drag skirt / backshell interface and a single order could be placed for all joints. The foreshell and emphasized design features are displayed in Figure 3 through Figure 6 below, and critical design parameters are tabulated in Table 1.

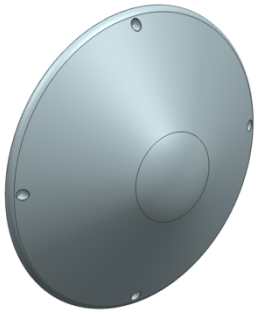

Figure 3. Foreshell Front Isometric View.

Figure 4. Foreshell Rear Isometric View.

Figure 5. Foreshell Side View.

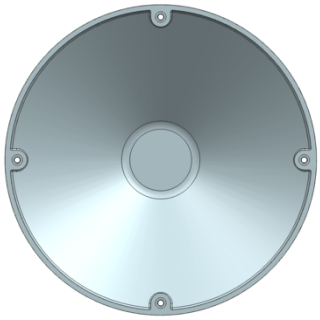

Figure 6. Foreshell (Aft Looking Forward).

Table 1. Foreshell Design Parameters.

Parameter	Value	Unit
r	10.0	cm
L_1	4.15	cm
θ	60.0	degrees
r_n	5.63	cm
r_s	0.56	cm
t	0.30	cm
$m_{foreshell}$	0.27	kg
C_DA	419.72	cm^2

The backshell was designed in parallel with the foreshell and includes the same four orthogonally spaced mating bosses, as well as the same 3 mm thickness 6061 aluminum. While the foreshell includes the male boss feature, the backshell was designated the female feature due to a greater amount of material being available such that local thickness limits did not become an issue. Upon selecting an attitude control system (ACS) and recognizing high internal heating challenges, it was decided to eliminate the aft face of the backshell and leave it open for ACS thruster, heat transfer, and static stability purposes. While this change slightly altered the machine process for the backshell manufacturing, it did not require any additional extraneous complications. Additionally, 4 symmetric slots were cut into the aft portion of the shell such that the antenna of choice (GOMSpace® NanoCom ANT430) could deploy in four orthogonal directions following atmospheric egress and transmit the recorded data taken during the entry, jettison and exit phases of the aerocapture sequence. The backshell and design features highlighted are displayed in Figure 7 through Figure 9 below, while critical design values are tabulated in Table 2.

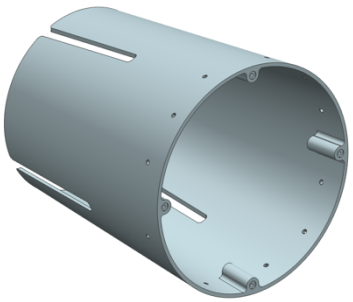

Figure 7. Backshell Isometric View.

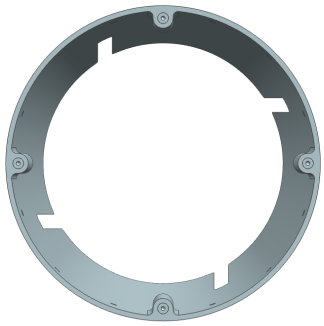

Figure 8. Backshell (Forward Looking Aft).

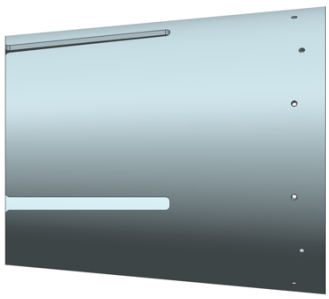

Figure 9. Backshell Side View.

Table 2. Backshell Design Parameters.

Parameter	Value	Unit
r	10.0	cm
r_b	7.50	cm
ψ	5.30	degrees
L_2	21.0	cm
t	0.30	cm
$m_{backshell}$	0.91	kg

While Section VII details the trades associated with the drag skirt configuration, the CAD design of the piece parts followed that of the foreshell and backshell. Intentionally made of identical material and thickness parameters as the foreshell and backshell, the drag skirt was simply designed as a radial extension of the 60° sphere cone defined by the foreshell. Four identical quadrants were designed with an acutely angled flange through which three fasteners secure the skirt sections to the backshell, as displayed in Figure 11 and Figure 12. Pertinent design parameters of the drag skirt sections are tabulated below in Table 3.

Table 3. Drag Skirt Design Parameters.

Parameter	Value	Unit
R	25.0	cm
θ	60.0	degrees
t	0.30	cm
$m_{drag\ skirt,\ quadrant}$	0.41	kg
C_DA	2945.24	cm^2

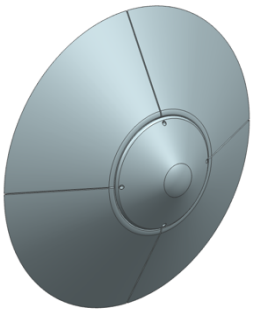

Figure 10. Drag Skirt Front Isometric View.

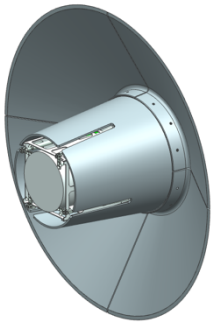

Figure 11. Drag Skirt Rear Isometric View.

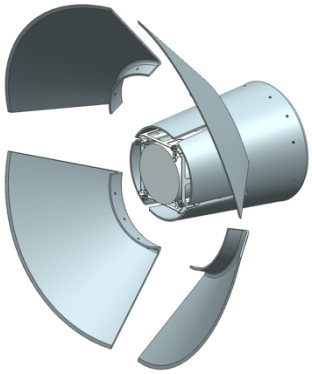

Figure 12. Post-Jettison Drag Skirt Rear Isometric View.

In order to minimize mass and maximize the impact of ballistic coefficient adjustment pre and post-jettison, it was initially envisioned to trade a series of lightweight materials for the drag skirt sections such as fiberglass, carbon fiber, high temperature thermoplastics and alternate metallic materials; however, further thought exposed how much complexity employing fiber reinforced composites introduced to the overall design, and additional challenges were introduced though the incorporation of plastic as a primary structural member. With that being said, for the sake of this initial study, aluminum was selected as the material to be used for manufacturing of the drag skirt sections.

In conjunction with the design of the three individual parts, the assembly sequence and payload interface design needed to be addressed. The assembly sequence for this vehicle is as follows:

- Connect drag skirt sections to backshell canister via 12 M3 / 7 mm pyrotechnic fasteners
- Join payload and foreshell at designated locations on both the interior foreshell and payload structure
- Join the backshell / drag skirt assembly with the foreshell / payload assembly via 4 M3 / 6 mm fasteners

VI. Static Stability Analysis

During the conceptual phase of design when the aeroshell geometry was indicative of Figure 13 and Figure 14, questions arose regarding both the static and dynamic stability of the vehicle due to the cylindrical nature of the backshell; because of this, both a literature review and CBAERO® analysis were conducted to provide closure to the questions. Per [5], the stability of a conical forebody with a cylindrical afterbody can be approximated as a function of longitudinal length and afterbody taper angle. This documentation highlighted the probability of a stability concern due to the lack of an afterbody taper immediately aft of the foreshell / backshell mating plane.

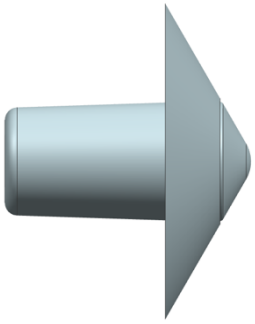

Figure 13. First Iteration Backshell Design (1).

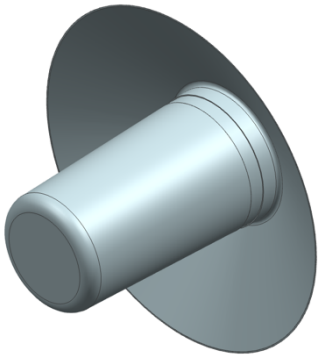

Figure 14. First Iteration Backshell Design (2).

Because of this, the payload geometry needed to be more properly defined and emphasis was placed upon minimizing the length and maximizing the taper angle of the conical afterbody. Additionally, a first order CG estimate and CFD analysis of the system needed to be conducted such that static stability derivatives and static margin values could be calculated and tabulated (Table 4) for discretized trajectory points in both the pre and post-jettison configurations. The resulting analysis revealed a very wide static margin for the pre-jettison configuration with a smaller, but still stable amount following the drag skirt jettison. Additional checks of nose-forward versus nose-aft static stability were made as well and are discussed in more depth in Section VIII.

Table 4. Pre & Post Jettison Static Margin Values.

Configuration	Time (s)	$\hat{x}$ (cm)
Pre-Jettison	0	N/A
	50	63.42
	100	58.99
	150	58.64
Post-Jettison	150	7.98
	200	8.52
	250	11.34
	300	-3.31
	350	-243.88
	400	N/A

As for the dynamic stability of the system, the highly hypersonic, high altitude and correspondingly low density flow flight regime led to the conclusion that the vehicle should remain in an oscillatory stable configuration throughout atmospheric interface; therefore, further analysis pertaining to the dynamic stability of the system was labeled as a minor priority and placed on hold for future work if necessary.

VII. Drag Skirt Structural Analysis

The primary structural concerns for the drag skirt design arose due to the nature of pressure loading on each quadrant which can be generally compared to that of a distributive load on a cantilevered section. The peak stresses occurring on the interior fillet needed to compared with critical material values, as they represented the highest priority critical design stresses. In order to analyze the geometry, an ANSYS® static structural analysis run was generated and completed first for an individual quadrant, followed by an assembly of four quadrants which took into account bondlines and compression boundary conditions. The first step in the process was calculating the total pressure load acting over the surface area of the drag skirt. Referring to Equations 2 and 3, peak static pressure occurs at approximately t = 150 s when the dynamic pressure and freestream pressure of the system reaches its maximum (in the pre-jettison configuration).

$$C_p = C_{p,max}\sin^2(\theta) = 2\sin^2(\theta) = \frac{P - P_\infty}{q_\infty} \tag{2}$$

$$P = C_p q_\infty + P_\infty \tag{3}$$

At this point in time, the static pressure on each quadrant equals approximately 6.4 kPa; applying this pressure to each section and fixing the base of each quadrant as a boundary condition yields the deformation and equivalent stress results for both the individual quadrant and entire drag skirt configuration, as displayed in Figure 15 through Figure 18, respectively.

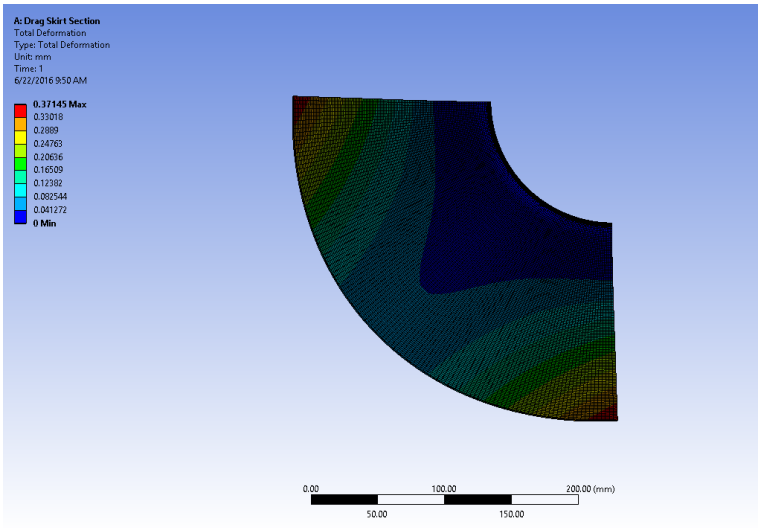

Figure 15. Single Quadrant Deflection Analysis.

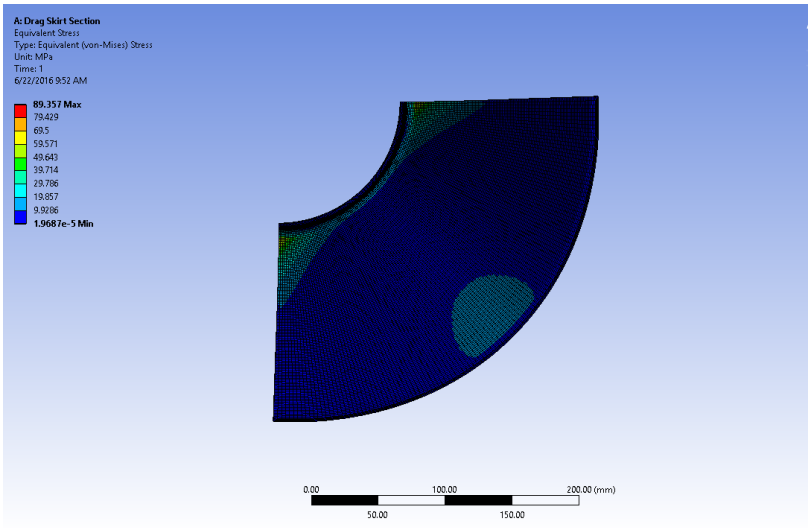

Figure 16. Single Quadrant von-Mises Stress Analysis.

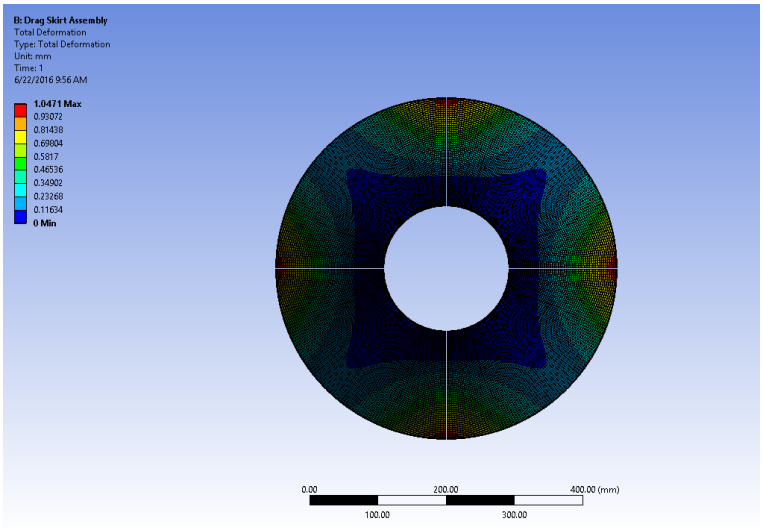

Figure 17. Drag Skirt Assembly Deformation Analysis.

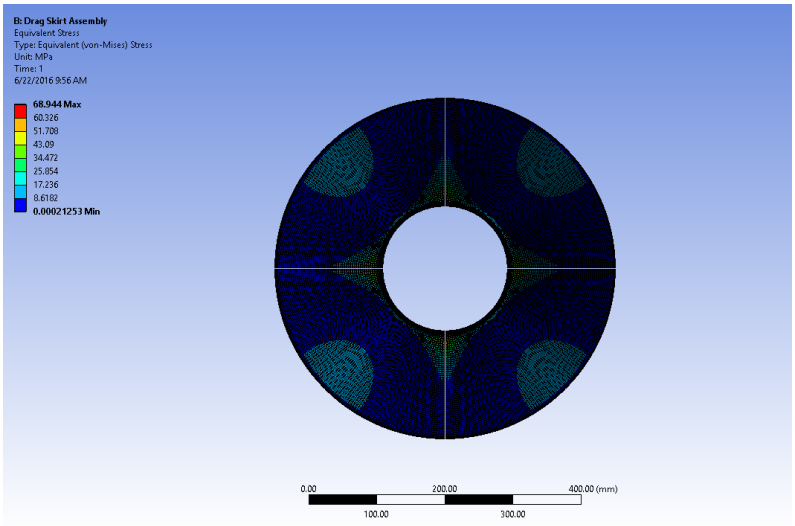

Figure 18. Drag Skirt Assembly von-Mises Stress Analysis.

Upon seeing that the stresses in each section were well below the critical yielding stresses for machined 6061 aluminum (~270 MPa), a mass savings optimization was performed to see whether or not the section thickness could be further reduced at the interior fillet; however, in order to maintain the primary objective of keeping all parts simply machineable, the mass savings for each quadrant only equated to 11 grams and the adjustment to the part geometry was deemed a minor priority which could be revisited if 44 grams of mass savings was required for mission eligibility.

VIII. Geometric Heating Analysis

The aeroshell geometry selection documented in Section IV directly effects the global heating parameters of the entry vehicle. Knowing the trajectory profile, the stagnation point heating could be easily obtained from the Sutton Graves approximation, as displayed in Equation 4.

$$\dot{q}_{stag} = K\sqrt{\frac{\rho}{r_n}}V_\infty^3 \tag{4}$$

This value allowed for a first order TPS sizing for the vehicle which resulted in approximately 4.2 cm of phenolic impregnated carbon ablator (PICA) around the entire vehicle; however, this is an extremely conservative approximation which significantly increases vehicle mass and drives the CG aft, which in turn decreases static stability. In order to obtain a better idea for heating along the hemispherical nose cap and forebody flank, as well as longitudinally along the afterbody, a literature review was conducted and four particular resources stood out which directly address forebody and afterbody heating of axisymmetric blunt bodies of revolution in hypersonic flow. For the hemispherical nose cap, the heating downstream of the stagnation point can be roughly compared to the stagnation point heating through Equation 5 below; however, this estimate becomes decreasingly valid as $\theta \rightarrow 90°$. It is useful to note that while Equation 5 is primary used for ($\theta < 45°$), it has been used in practice for values of θ up to 70° and has been tested for a variety of conical half angles exceeding 45°.

$$\frac{\dot{q}}{\dot{q}_{stag}} \approx \cos(\theta) \tag{5}$$

Three separate approaches were used to better estimate heat flux values along the 60° conical flank; the first approach employed theory proposed by Lester Lees in the late 1950's which relates the conical flank heat flux to the stagnation point heating through Newtonian flow relationships solely dependent upon freestream Mach Number, the applied gas constant (γ_∞) and the conical flank angle; while a thorough derivation of this relationship is provided in [6], the results are plotted and displayed in Figure 19.

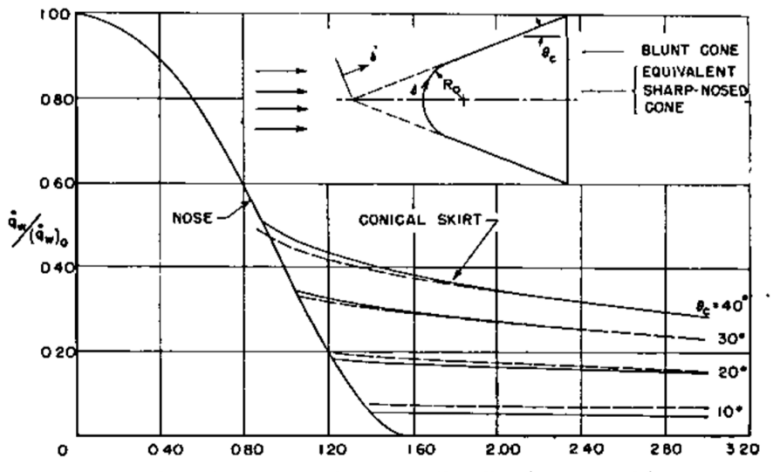

Figure 19. Conical Flank Heat Flux Estimations (Lees).

Supplementary information to the aforementioned forebody heating theory can be found in [7] where experimental data was compared against Lees' approximations. The results of the experiment closely matched those of the theoretical relationships; geometric definitions and resulting heat flux distributions are displayed in Figure 20 and Figure 21, respectively.

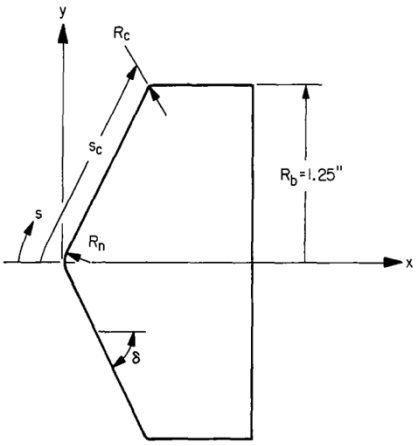

Figure 20. Blunted Cone Forebody Heat Flux Variable Definition.

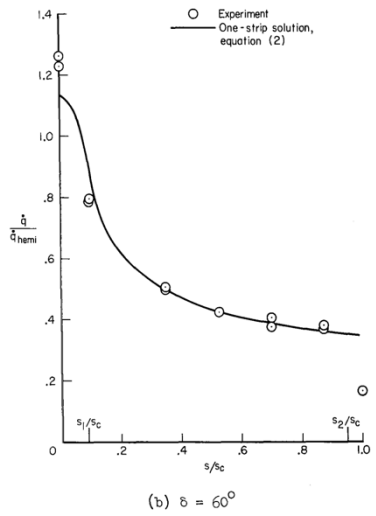

Figure 21. Blunted Cone Forebody Heat Flux Scaling Parameter.

The third approach taken to help better estimate the downstream forebody heat flux employed data from heritage missions of similar geometry and entry corridor (i.e. Stardust, Genesis). Computational heating estimations were

performed by Roop N. Gupta at NASA LaRC prior to the Stardust mission in the late 1990's [8] which indicated similar relationships to those obtained in the previous explanations; fortunately, the computational data also accounted for laminar and turbulent transitions in the forebody flow field, as well as the effects of ablative and non-ablative TPS materials. A geometric definition of the Stardust capsule and forebody heat flux estimations are displayed in Figure 22 and Figure 23, respectively.

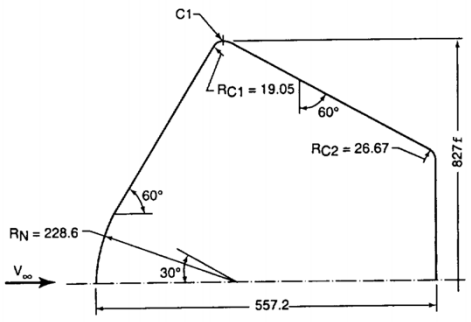

Figure 22. Stardust Capsule Geometry Definition.

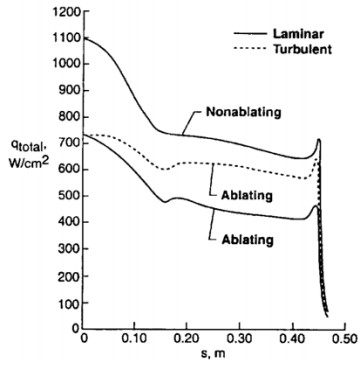

Figure 23. Stardust Capsule Forebody Heat Flux.

The accumulation of these theoretical, experimental and computational heating estimations applied to a 60° conical flank yielded the result that the heat flux along the conical frustum could be approximated to be somewhere between 45% and 65% of that seen at the stagnation point, dependent upon assumptions made regarding radiative heat flux contributions, boundary layer properties and TPS material selection.

Reference [9] documents a series of tests which were completed for the Aeroassist Flight Experiment (AFE) in 1990. While AFE's foreshell wasn't an axisymmetric body of revolution, the lower half plane of the forebody was a 60° sphere cone with a trailing cylindrical afterbody, and testing condition Reynolds Numbers were near what would be anticipated for the cubesat trajectory. The testing configuration with all defined variables is displayed in Figure 24 through Figure 26 below.

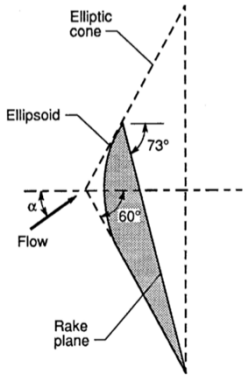

Figure 24. AFE Foreshell Geometry.

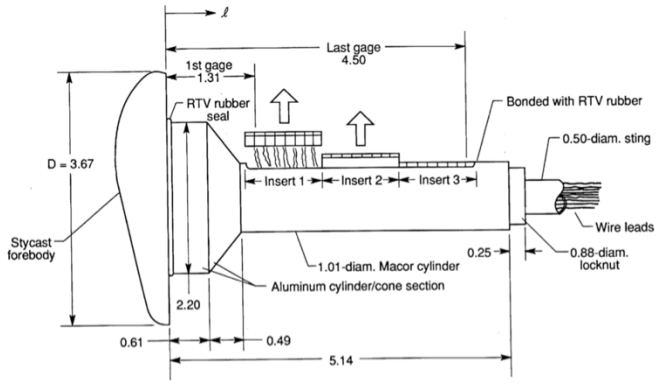

Figure 25. AFE Afterbody Heating Experimental Setup.

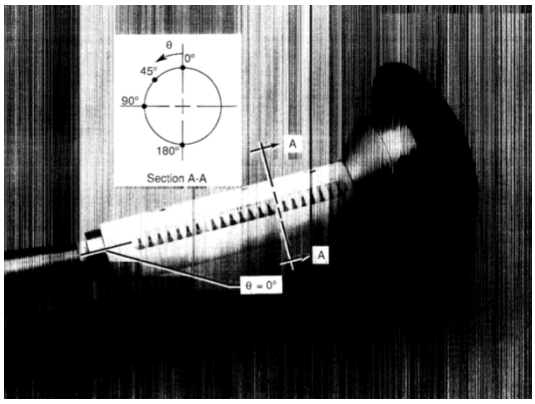

Figure 26. AFE Afterbody Heating Experimental Setup Parameter Definition (θ).

While a much more in-depth review can be found in [9], the results indicated that heat flux values along the backshell were approximately 10% of those seen at the stagnation point; therefore, the amount of TPS necessary for the backshell could be resized to reflect the much lower anticipated heating values.

In addition to the AFE documentation, [10] documents both analytic and experimental results of afterbody heating estimations for a 70° sphere cone forebody aeroassist entry vehicle. While the foreshell geometry is different, the independent conclusions drawn from this study were that the freestream Stanton Number (St_∞) could be approximated as a function of longitudinal position (X) relative to radial distance inboard of the foreshell outer diameter (h), and that the ballistic coefficient had a significant impact on afterbody heating approximations functionally dependent on

the same relationship, as displayed in Figure 27 through Figure 29. Note that for the aforementioned geometry and heat shield material, the value of $\left(\frac{X}{h}\right) \approx 0.9$ and remains within that domain due to the backshell taper.

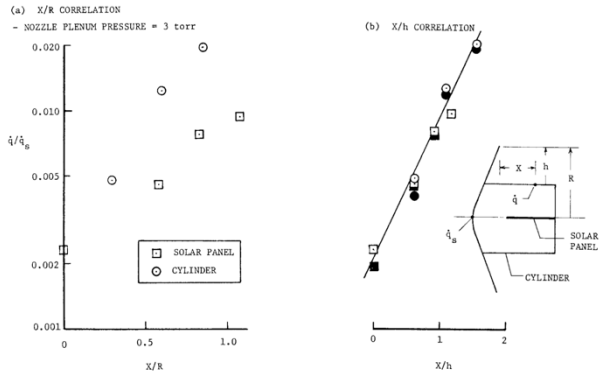

Figure 27. Cylindrical Afterbody Heat Flux Relationship.

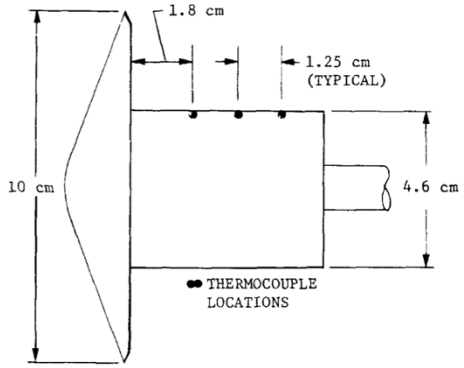

Figure 28. Cylindrical Afterbody Heating Experimental Setup.

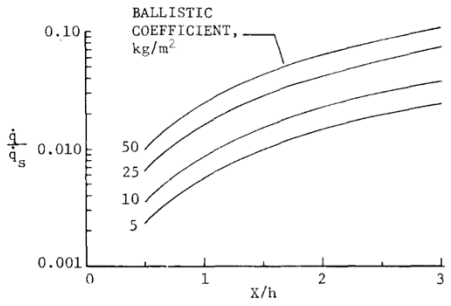

Figure 29. Cylindrical Afterbody Heating Dependence on Ballistic Coefficient.

This correlation could be directly fed back to provide additional data for afterbody TPS sizing. These resources allowed for a secondary TPS sizing to be conducted for the vehicle, resulting in a TPS thickness reduction of nearly 4.3% on the forward flank and 17.1% on the backshell.

IX. Drag Skirt Jettison Mechanism

A primary focus of this study was to conceive and design the mechanical system which actually performs the hypersonic drag modulation previously explained. Initial concepts were broken into the previously mentioned two

architectures: discrete single-stage modulation and variable actuation modulation. While more advanced vehicles could greatly benefit from having the option to tailor *in situ* drag (and lift) properties during entry, the higher order goal of maintaining mission simplicity drove the selection of a rigid, single-stage system with which to alter the vehicle's ballistic coefficient and clearly demonstrate aerocapture. Following the decision to proceed with a rigid system, the second trade study involved the discretization of the structure. The three options were as follows: one complete body of revolution, two semicircle sections, or four quadrants. Each option had its own positive and negative aspects; however, upon weighing the potential risks and benefits of all three choices it was decided to proceed with the four quadrant concept, as it posed the least amount of risk and could be manufactured with the minimal amount of machine constraints. The one key risk of the discretized design that arose concerned the nature of the aerodynamic pressure loading on the drag skirt aero surfaces and the overturning moment imparted on each section following detachment from the primary aeroshell assembly. In order to quantify this problem to a first order degree, a 2D dynamic analysis of a skirt section was attempted which would generate at least 9 dynamic equations of motion for the skirt as a function of its rotation angle ψ in order to confirm that by the time ψ = 185.3° (equal to the backshell's taper angle), the aeroshell assembly would be free and clear from an impact. Assuming Newtonian flow on all hypersonic aero surfaces, the problem needed to be discretized into three separate time domains, as displayed in Figure 30 through Figure 32 below.

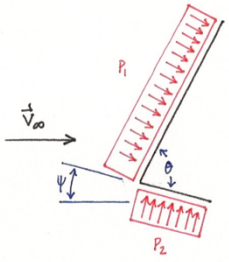

Figure 30. Post-Jettison Drag Skirt Dynamics (Configuration 1).

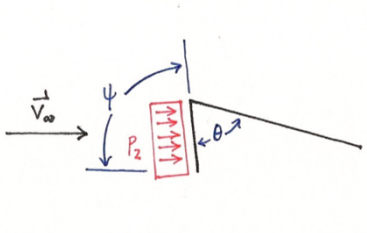

Figure 31. Post-Jettison Drag Skirt Dynamics (Configuration 2).

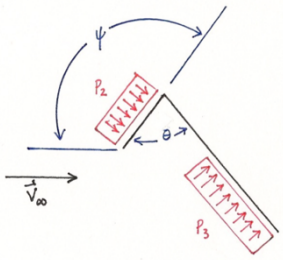

Figure 32. Post-Jettison Drag Skirt Dynamics (Configuration 3).

The initial time span took into consideration aero loads on both the flange and the flank, both of which are dependent on the rotation angle ψ. The second time domain considered the time when the entire flank is in the shadow region of the flange (65.3° < ψ < 75.4°) and the only aero loads acting on the body are those acting on the flange. The

third time domain covered the remainder of the initial trajectory when the backside of the flank rotates through the flange's shadow region and generates a counter-rotating aero force. Following this time, it was hypothesized that the vehicle would experience oscillatory behavior, then tend toward a stable configuration where the relative aero forces on the flange and flank balance; however, this was only an educated guess, and could be examined further as noted in Section XII.

Upon undertaking this task, it was soon realized that the combination of assumptions being made regarding hypersonic shock interactions, ideal Newtonian flow properties and rigid body dynamics coupled with the level of complexity required to converge on a simplified solution necessitated a different approach to the drag skirt jettison problem. Instead, the question of how stable the configuration would be *even if* the drag skirt section made contact with the backshell, and at what angle of attack would the vehicle lose its pitching stability was addressed. In order to answer this question, the pitching moment stability derivative $\left(C_{m_\alpha}\right)$ was plotted as a function of angle of attack to see how perturbed the post-jettison configuration could become before becoming unstable; Figure 33 below displays this behavior, which indicated that the post-jettison vehicle configuration could safely withstand a perturbation angle of attack of approximately 57.5° before becoming statically unstable. Upon exceeding this critical value of α, the vehicle would unstably rotate about the y-axis and return to its stable range of angles of attack ($-57.5° \lesssim \alpha \lesssim 57.5°$). As previously mentioned, the aft face on the backshell was intentionally removed for static stability reasons; this geometric alteration significantly reduces the risk of a nose-aft stability mode which is common for blunt body entry vehicles [11]; Figure 33 also displays this trend, as the value of C_{m_α} is distinctly positive at $\alpha = 180°$.

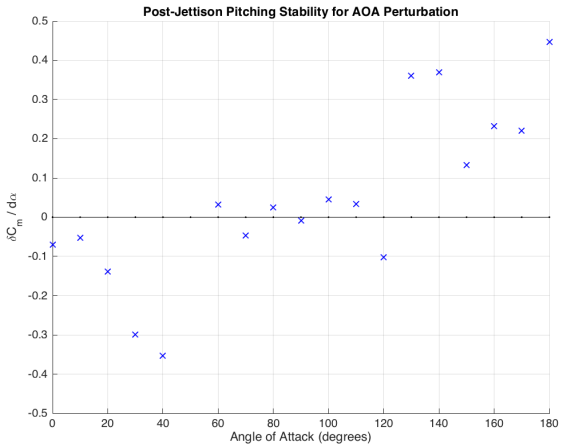

Figure 33. Post-Jettison Pitching Stability.

The next question to be answered was that of the actuation device to be employed to separate the two components. A vast majority of heritage NASA missions have employed pyrotechnic devices, so pyrotechnic NASA Standard Initiator (NSI) M3 break bolts were chosen to both fasten and release the drag skirt from the aeroshell, as displayed in Figure 34. Additionally, shear load bolt sizing was conducted in conjunction with the previously calculated aerodynamic loads on the drag skirt; the results indicated that the peak fastener stresses were far below that of any material yielding properties, so three per quadrant was deemed sufficient with the possibility to reduce fastener size.

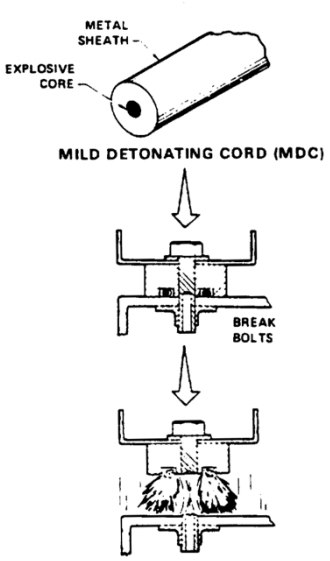

Figure 34. Pyrotechnic Break Bolt Mechanics.

The advantageous properties of NSI relative to other options includes its stability with regards to pressure and temperature, predictable delay for detonation, long shelf life and minimal gas output; however, it is electrostatically sensitive and emits hot particles, both risks which need to be taken into account prior to use. A much more in-depth discussion regarding pyrotechnic actuators can be found in [12].

X. Host Vehicle Interface Bracket

Interface with the host vehicle was an important design parameter to address as the spin-stabilization provided from the host significantly aids in the entry vehicle's stability throughout the trajectory. Because a wide range of heritage missions have employed the use of the Planetary Systems Corporation Mark II Motorized Lightband®, it was

selected to be the interfacing piece of hardware for this mission. While [13] provides a detailed specification sheet, the 8-inch bolt circle diameter Lightband of choice is essentially a series of two concentric rings that interface through a series of actuated pin pullers which activate and separate at a specified time; this splits the assembly into its two components, one of which remains with the host while the other remains with the entry vehicle. Four orthogonally spaced L-brackets were designed to provide attachment between the remaining portion of the Lightband and the backshell of the entry vehicle. Similar to the drag skirt jettison design, the mechanical joint between the L-brackets and backshell is via four pyrotechnic bolts which fire exo-atmospherically and separate the remaining Lightband from the entry vehicle. Figure 35 displays the joint Lightband assembly while Figure 36 displays its interface with the aeroshell.

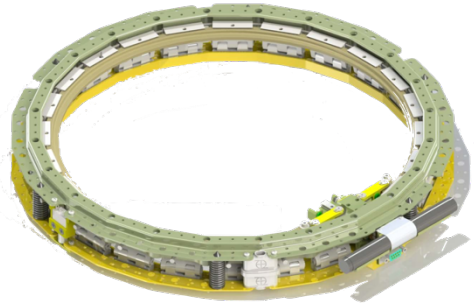

Figure 35. Generic Lightband Assembly.

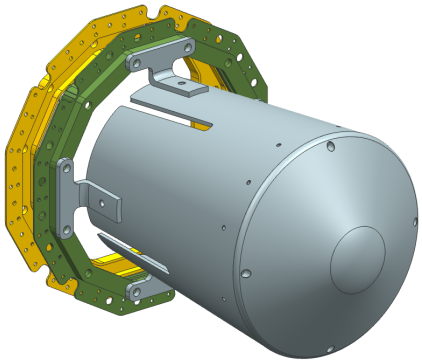

Figure 36. 8" Lightband Interface with Backshell.

XI. Prototyping

In order to obtain a visual representation of the entry vehicle design, two separate stages of prototyping were conducted. While still in the early stages of conceptual design, an initial iteration of the entry vehicle (Figure 13 & Figure 14) was 3D printed from ABS plastic in order to get a sense of the backshell's taper and longitudinal extension in the aft direction. This print, as displayed in Figure 37 and Figure 38, was a valuable tool within the design process as it exposed and confirmed outstanding questions regarding the afterbody's effect on static stability.

Figure 37. First Iteration 3D Print (1).

Figure 38. First Iteration 3D Print (2).

The second iteration of prototyping had initially aimed to be machined out of aluminum at a one-half scale size; however, due to cost and time constrains, the design was instead 3D printed, only this time from a combination of stainless steel and alumide metallic plastic. The resulting prototype aimed to address machine tool design, assembly, tolerance, and cost. Displayed in Figure 39 and Figure 40 are images of the resulting print and assembly of the most recent entry vehicle design iteration.

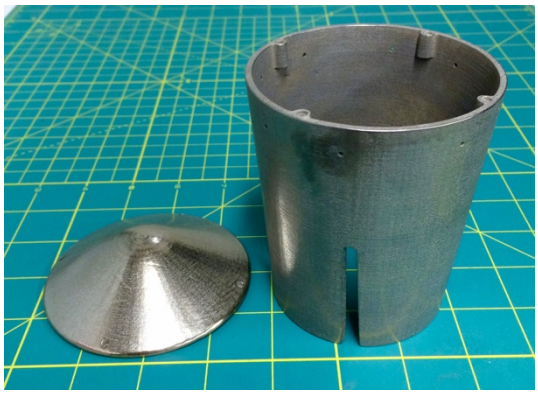

Figure 39. Second Iteration Aeroshell Prototype (1).

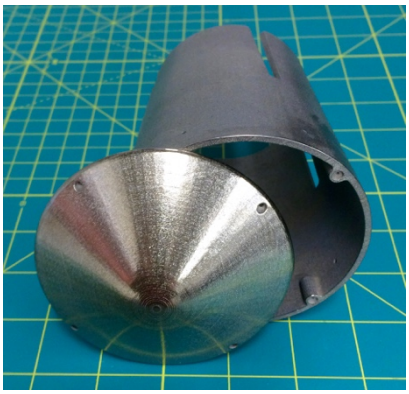

Figure 40. Second Iteration Aeroshell Prototype (2).

For future reference, let it be noted that the initial quote per the selected machine shop for a one-half scale model of the entire entry vehicle, machined out of 6061 aluminum stock, was between $6,000 and $10,000 with a lead time of 1-2 months.

XII. Future Work

While a great deal of progress was made to this point advancing this particular aerocapture aeroshell design, there is still plenty more that can be examined in order to further refine the level of understanding for this concept. A few key examples include:

- design of a mechanism that secures the payload to the aeroshell which accounts for launch vibration and structural loads
- validation of the designed interface between the aeroshell and the host vehicle
- optimize and analyze the static CG location in order to generate a sufficient amount of static margin throughout the entire trajectory
- complete a more thorough investigation for potential drag skirt materials and manufacturing techniques with primary goals focused on mass savings and manufacturing cost / time
- further refine heating estimates and associated TPS distributions through computational simulation
- generate both 2D and 3D skirt jettison dynamic models with which to address jettison event risk
- build and test pyrotechnic jettison devices in order to verify analysis from derived models

XIII. Concluding Remarks

As previously stated, aerocapture entry vehicles provide a great amount of potential for future missions not only in terms of payload mass fraction, but more importantly in lieu of mission facilitation for the planets on the outer edge of the Solar System where aerocapture is the only possible way to capture orbit. The study conducted throughout this document aimed to advance a technology that is believed to pose the greatest possibility of a near-future aerocapture demonstration. It has been shown through the contents of this study that single-stage drag modulated aerocapture can indeed be demonstrated at Earth for a relatively low cost and low risk by means of a smallsat entry vehicle. The proposed system would only require approximately 20 kg and 0.1 m^3 of secondary payload mass and volume, respectively, but would provide so much more in terms of proving a concept which shows great potential for future planetary exploration. The system complexity required by the aeroshell, jettison mechanism and flight hardware was designed in such a way that multiple configurations could be flown and tested against one another to verify mission repeatability and help better understand the aspects of aerocapture that may not be uncovered until actual flight. While

there is still plenty of work required to advance the proposed technology, the concept shows a great deal of potential for performing single-stage drag modulated aerocapture on a small scale. If aerocapture is ever to be used for a flagship mission, it would be very beneficial to have flown a similar trajectory at a smaller scale in order to better understand the requirements of a true aerocapture mission.

XIV. Acknowledgements

The first author would like to thank Dr. Robert D. Braun and the Georgia Institute of Technology Space Systems Design Laboratory (SSDL) for the opportunity to conduct the research documented above. Additionally, the first author would like to thank all colleagues at the Jet Propulsion Laboratory (JPL) in Pasadena, CA for their efforts toward this study.

XV. References

[1] Putnam, Z. R., "Improved Analytical Methods for Assessment of Hypersonic Drag-Modulation Trajectory Control," PhD Dissertation, Georgia Institute of Technology, March 2015.

[2] Putnam, Z. R., and Braun, R. D., "Precision Landing at Mars Using Discrete Event Drag Modulation," *Journal of Spacecraft and Rockets*, Vol. 51, No. 1, Feb. 2014.

[3] Mitcheltree, R. A., Moss, J. N., Cheatwood, F. M., Greene, F. A., and Braun, R. D., "Aerodynamics of the Mars Microprobe Entry Vehicles," *Journal of Spacecraft and Rockets*, Vol. 36, No. 3, 1999.

[4] Karpov, B. G., "The Effect of Various Boattail Shapes on Base Pressure and other Aerodynamic Characteristics of a 7-Caliber Long Body of Revolution at M = 1.70," *Ballistic Research Laboratories* Report No. 1295, Aug. 1965.

[5] Charwat, A. F., "The Stability of Bodies of Revolution at Very High Mach Numbers," *Journal of Jet Propulsion*, Vol. 27, No. 8, 1957.

[6] Lees, L., "Laminar Heat Transfer Over Blunt-Nosed Bodies at Hypersonic Speeds," *Journal of Jet Propulsion*, Vol. 26, No. 4, 1956.

[7] Stewart, D. A., and Marvin, J. G., "Convective Heat Transfer Rates on Large-Scale Conical Bodies at Hypersonic Speeds," NASA TN D-5526, Nov. 1969.

[8] Gupta, R. N., "Aerothermodynamic Analysis of Stardust Sample Return Capsule with Coupled Radiation and Ablations," *Journal of Spacecraft and Rockets*, Vol. 37, No. 4, Jul. 2000.

[9] Wells, W. L., "Surface Flow and Heating Distributions on a Cylinder in Near Wake of Aeroassist Flight Experiment (AFE) Configuration at Incidence in Mach 10 Air," NASA TP-2954, Jan. 1990.

[10] Schmitt, D. A., "Base Heating on an Aerobraking Orbital Transfer Vehicle," *AIAA 21st Aerospace Sciences Meeting*, AIAA 1983-0408, Jan. 1983.

[11] Mitcheltree, R., Hughes, S., Dillman, R., and Teter, J., "An Earth Entry Vehicle for Returning Samples from Mars," AAAF Paper ARVS-102, Mar. 2001.

[12] Bement, L. J., and Schimmel, M. L., "A Manual of Pyrotechnic Design, Development and Qualification" NASA TM-110172, Jun. 1995.

[13] Planetary Systems Corporation, "2000785F MkII MLB User Manual," Jul. 2014.